J Nanopart Res
DOI 10.1007/s11051-009-9695-x

SPECIAL FOCUS: SAFETY OF NANOPARTICLES

Monitor for detecting and assessing exposure to airborne nanoparticles

Johan Marra · Matthias Voetz · Heinz-Jürgen Kiesling

Received: 10 June 2009 / Accepted: 24 June 2009
© Springer Science+Business Media B.V. 2009

Abstract An important safety aspect of the workplace environment concerns the severity of its air pollution with nanoparticles (NP; <100 nm) and ultrafine particles (UFP; <300 nm). Depending on their size and chemical nature, exposure to these particles through inhalation can be hazardous because of their intrinsic ability to deposit in the deep lung regions and the possibility to subsequently pass into the blood stream. Recommended safety measures in the nanomaterials industry are pragmatic, aiming at exposure minimization in general, and advocating continuous control by monitoring both the workplace air pollution level and the personal exposure to airborne NPs. This article describes the design and operation of the Aerasense NP monitor that enables intelligence gathering in particular with respect to airborne particles in the 10–300 nm size range. The NP monitor provides real time information about their number concentration, average size, and surface areas per unit volume of inhaled air that deposit in the various compartments of the respiratory tract. The monitor's functionality relies on electrical charging of airborne particles and subsequent measurements of the total particle charge concentration under various conditions. Information obtained with the NP monitor in a typical workplace environment has been compared with simultaneously recorded data from a Scanning Mobility Particle Sizer (SMPS) capable of measuring the particle size distribution in the 11–1086 nm size range. When the toxicological properties of the engineered and/or released particles in the workplace are known, personal exposure monitoring allows a risk assessment to be made for a worker during each workday, when the workplace-produced particles can be distinguished from other (ambient) particles.

Keywords Nanoparticles · Ultrafine particles · Workplace monitoring · Nanoparticle monitor · Ultrafine particle monitor · Occupational health · Instrumentation · EHS

List of symbols

A_0	A parameter defined in Eq. 13
C_1	A proportionality factor defined in Eq. 7
C_2, C_3	Proportionality factors defined in Eq. 19
C_{AL}	A proportionality factor defined in Eq. 26
$C_c(d_p)$	The Cunningham slip factor defined by $C_c(d_p) = 1 + \frac{\lambda}{d_p}\left(2.284 + 1.116 \exp\left(\frac{-0.5 d_p}{\lambda}\right)\right)$ wherein $\lambda = 0.066 \times 10^{-6}$ m, the mean free path of air molecules at atmospheric pressure (1 atm) and 20 °C

J. Marra (✉)
Philips Research Laboratories, HTC 4,
5656 AE Eindhoven, The Netherlands
e-mail: johan.marra@philips.com

M. Voetz · H.-J. Kiesling
Bayer Technology Services, Leverkusen, Germany

Published online: 15 July 2009

d_p	The particle diameter (m)
$d_{p,av}$	The number-averaged particle diameter (m)
$d^*_{p,av}$	The assumed (default) number-averaged particle diameter (m)
d_0	The particle diameter at which $\xi_q(d_p,E_{pl}) = 1$ for $d_p \leq d_0$ and $q \geq 1$ at the chosen electrical field strength E_{pl} (m)
d_{pl}	The spacing between the electrode surfaces in the precipitation section (m)
$D_{AL}(d_p)$	The fractional deposition efficiency of an inhaled particle of diameter d_p in the alveolar region
$D_{HA}(d_p)$	The fractional deposition efficiency of an inhaled particle of diameter d_p in the head airways
$D_{TB}(d_p)$	The fractional deposition efficiency of an inhaled particle of diameter d_p in the tracheo-bronchial region
e	The elementary charge ($e = 1.6 \times 10^{-19}$ C)
E_{pl}	The applied electrical field strength between the electrode surfaces in the precipitation section (V/m)
$f_q(d_p)$	The fraction of all particles of diameter d_p charged with "q" elementary charges
I_{sensor}	The electrical current signal measured by the NP monitor (A)
I_1	The measured electrical current signal when $V_{pl} = 0$ in the monitor's precipitation section (A)
I_2	The measured electrical current signal when $V_{pl} = V_1$ in the monitor's precipitation section (A)
L	The particle length concentration defined by $L = Nd_{p,av}$ (m/m^3)
L_{pl}	The traveling length of the electrode surfaces in the precipitation section
N	The total particle number concentration (particles/m^3)
N_{app}	The inferred apparent particle number concentration when a default average particle diameter $d^*_{p,av}$ is assumed to exist (see Eq. 8) (particles/m^3)
$N(d_p)$	The number concentration of particles of diameter d_p (particles/m^3)
N_{ion}	The number concentration of airborne ions in the particle charging section (ions/m^3)
$(Nd_{p,av})_0$	The safe threshold particle length concentration (particles m^{-3} m)
P	The air pollution index number defined in Eq. 29
q	The number of elementary charges on a particle
$Q(d_p)$	The average number of elementary charges on a particle of diameter d_p
S_{dp}	A proportionality factor defined in Eq. 17
S_N	A proportionality factor defined in Eq. 15
S_{Napp}	A proportionality factor defined in Eq. 9
S_{AL}	The deposited particle surface area per unit volume of inhaled air in the alveolar region (m^2/m^3)
S_{HA}	The deposited particle surface area per unit volume of inhaled air in the head airway region (m^2/m^3)
S_{TB}	The deposited particle surface area per unit volume of inhaled air in the tracheo-bronchial region (m^2/m^3)
t_r	The exposure time of airborne particles to airborne ions in the particle charging section (s)
v_{air}	The average air speed between the electrode surfaces in the precipitation section (m/s)
V_{pl}, V_1	The applied voltage difference between the electrode surfaces in the precipitation section (V)
σ	The size distribution parameter
ϕ	The airflow through the NP monitor (m^3/s)
ϕ^*	The reference airflow through the NP monitor (m^3/s)
$\xi_q(d_p,E_{pl})$	The fractional degree of precipitation of particles of diameter d_p charged with "q" elementary charges under the influence of an applied electrical field strength E_{pl}
η_{air}	The viscosity of air ($\eta_{air} = 1.8 \times 10^{-5}$ Pa.s)

Introduction

The potential benefits of nanotechnology for society are well-recognized by now, but there is also increasing awareness about uncertainties concerning the risk of released nanoparticles to the environment and human health. Questions in this regard have been posed by stakeholders in the nanotech industry and by several societal organizations, notably workers unions,

insurers, investment firms, NGO's, and governmental agencies (Balbus et al. 2007). Of particular importance is the potential hazard to the health of workers employed by the nanomaterials industry where products are made comprising engineered nanoparticles (NP). Depending on their size and chemical nature, exposure to NPs through inhalation can be hazardous because of their ability to reach and deposit in the deep alveolar region of the lung from where they may subsequently enter the systemic circulation (Kreyling et al. 2002; Oberdörster et al. 1995). NPs deposited in the nose may create additional hazard through their potential ability to transfer to the brain via the olfactory nerve (Elder et al. 2006). Studies with engineered NPs demonstrated their ability to cross the blood-brain and blood-testis barriers and the nuclear membrane inside cells, although it remains unknown to which extent this can eventually affect human health (Oberdörster 2004; Shosaku 2006; Kim et al. 2006; Geiser et al. 2005). Far more knowledge about adverse health effects is available from numerous studies with inhaled combustion-related fine particles ($\leq$10 μm or $\leq$2.5 μm) and ultrafine particles (UFPs, <300 nm), which are in the same size range as engineered NPs (Balbus et al. 2007). This knowledge is useful to guide risk studies with regard to engineered NPs but cannot replace them.

Shape, size, and chemical composition of a specific NP determine its intrinsic toxicity (hazard) and this may be quite different for different kinds of NPs. The health risk of NP intake is determined by both hazard and exposure. It has been recognized in comparative experiments that the airborne particle mass concentration is not a suitable metric for correlating NP exposure to health risks because this metric does not explicitly account for the finding that the toxicity of NPs and UFPs can be higher than the toxicity of fine particles per unit particle mass. For TiO_2 particles, particle toxicity was found to correlate much better with the inhaled particle surface area than with the inhaled particle mass (Oberdörster et al. 2005). Particle number concentration, particle surface area concentration and, more specifically, the particle surface area concentration in the inhaled air that deposits in the respiratory tract are believed to be more appropriate metrics for quantifying exposure to NPs and UFPs (Oberdörster 1996; Donaldson et al. 1998; Fissan et al. 2007).

The present article deals primarily with exposure assessment. A discussion is given about the technology comprised in the Aerasense NP monitor with which the particle number concentration N and the number-averaged particle size $d_{p,av}$ of airborne UFPs in the 10–300 nm size range can be determined. It will be explained how from a knowledge of N and $d_{p,av}$ or of the product $Nd_{p,av}$, it is possible to estimate the particle surface area concentrations in inhaled air that deposit in various regions of the respiratory tract.

The Aerasense NP monitor can be embodied as either a portable or a wall-mounted device for assessing the momentary and accumulated exposure of a worker to airborne NPs during a workday. Alternatively, the monitor can be used to assess the indoor or outdoor UFP pollution level, to guard the workplace environment, to trace particle sources, to trigger ventilation on demand via a feedback loop, and to assess the effectiveness of installed air filters or other measures intended to reduce exposure.

The Aerasense NP monitor

Principle of operation

A schematic picture of the Aerasense NP monitor is shown in Fig. 1. A controlled airflow ϕ is drawn via the inlet through the monitor by means of a fan situated atop the sensor. After entry, airborne particles are electrically charged inside the charging section via diffusion charging (Hinds 1999). Diffusion charging is enabled by a corona discharge from a needle-tip electrode that is set at a sufficiently high voltage V_{cor} to locally ionize the air. The needle-tip electrode is surrounded by a screen electrode, whereupon a screen voltage $V_{scr} \ll V_{cor}$ is imposed. Particle charging occurs in the air conduit between the screen electrode and the outer wall by contacting the particles with ions that move from the screen electrode across the conduit toward the opposite wall. The space-averaged ion concentration N_{ion} and the residence time t_r of the particles in this conduit determine the charging parameter, $N_{ion}t_r$ used in the Fuchs theory for quantifying particle diffusion charging (Adachi et al. 1985). V_{scr} is set at a voltage sufficiently high to prohibit ion escape from the charging section, yet low enough to avoid field charging and particle precipitation during particle charging.

After charging, the particles enter the precipitation section, wherein a block-shaped voltage pulse varying between $V_{pl} = V_1$, and $V_{pl} = 0$ is imposed

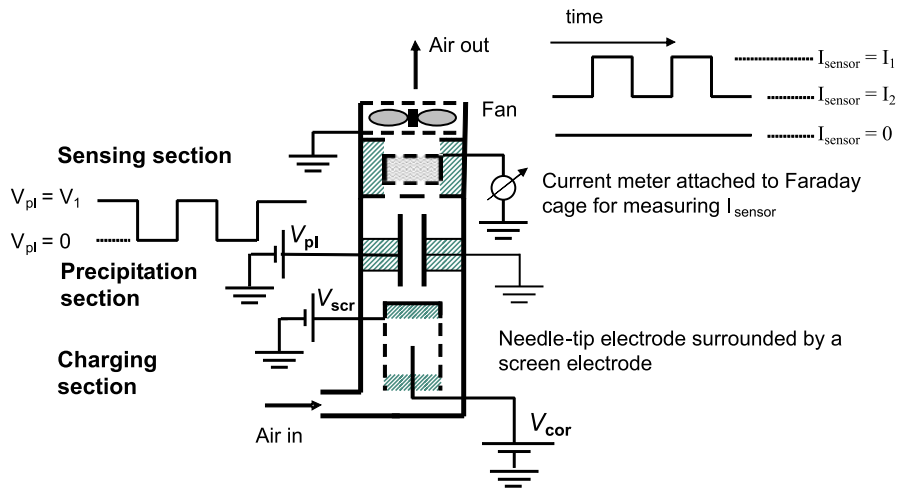

Fig. 1 Schematics of the Aerasense NP monitor

between two parallel electrode plates separated by a distance d_{pl}. At $V_{pl} = 0$, charged particles traverse the precipitation section unhindered. They are subsequently captured in a filter disposed inside an electrically isolated Faraday cage that is connected via a sensitive current meter to a reference potential. The current meter, having a sensitivity of about 1 fA, records the total particle charge that deposits per unit time inside the Faraday cage as an electrical current $I_{sensor} = I_1$. The current I_{sensor} constitutes the sensor signal. I_1 accounts for the charge of all airborne particles entering the Faraday cage according to

$$I_{sensor} = I_1 = \int_{d_p=0}^{\infty} \sum_{q=0}^{\infty} qe\phi f_q(N_{ion}t_r, d_p) \times \frac{dN(d_p)}{d\ln(d_p)} d\ln(d_p) \quad (1)$$

where, d_p represents the particle mobility diameter, "q" is the number of elementary charges on a particle, "e" is the elementary electron charge, $f_q(N_{ion}t_r, d_p)$ the fraction of all particles of diameter d_p that are charged with q elementary charges at the pertaining $N_{ion}t_r$, and $N(d_p)$ denotes the number concentration of particles with a diameter d_p. The total particle number concentration N relates to $N(d_p)$ according to

$$N = \int_{dp=0}^{\infty} \frac{dN(d_p)}{d\ln(d_p)} d\ln(d_p). \quad (2)$$

The integrals in Eqs. 1 and 2 extend across all particle sizes; however, it is well known that the overwhelming majority of airborne particles in ambient air are smaller than 300 nm and mostly even smaller than 100 nm. Larger particles will therefore in most cases not noticeably contribute to I_{sensor} and/or N.

At $V_{pl} = V_1$, at least some charged particles precipitate inside the plate section due to the field strength $E_{pl} = V_1/d_{pl}$ between the plates. All remaining particles are captured in the Faraday cage, giving rise to a second sensor signal

$$I_{sensor} = I_2 = \int_{d_p=0}^{\infty} \sum_{q=0}^{\infty} qe\phi f_q(N_{ion}t_r, d_p) \times \left[1 - \xi_q(d_p, E_{pl})\right] \frac{dN(d_p)}{d\ln(d_p)} d\ln(d_p) \quad (3)$$

wherein, $\xi_q(d_p, E_{pl})$ denotes the fractional precipitation of particles of diameter d_p charged with "q" elementary charges. Figure 1 shows that I_1 and I_2 are recorded sequentially. Laminar flow conditions are ensured to exist in the precipitation section, allowing $\xi_q(d_p, E_{pl})$ to be described according to

$$\begin{aligned} &\xi_q(d_p, E_{pl}) = 1, \quad \text{when} \\ &\frac{qeC_c(d_p)E_{pl}L_{pl}}{3\pi\eta_{air}d_p v_{air}d_{pl}} \geq 1 \quad \text{(full precipitation)}, \\ &\xi_q(d_p, E_{pl}) = \frac{qeC_c(d_p)E_{pl}L_{pl}}{3\pi\eta_{air}d_p v_{air}d_{pl}}, \quad \text{otherwise} \end{aligned} \quad (4)$$

$C_c(d_p)$ denotes the Cunningham slip factor, L_{pl} the traveling length of the parallel electrode plates, η_{air} the viscosity of air, and v_{air} the average air speed between the plates.

Inferring the particle length concentration L

The Fuchs theory is well-recognized to reliably predict particle diffusion charging behavior (Adachi et al. 1985) and can be used to obtain upfront quantitative insight in the fractional values $f_p(N_{ion}t_r,\ d_p)$. This enables the average number of elementary charges $Q(d_p)$ on a particle of diameter d_p to be inferred from

$$Q(d_p) = \sum_{q=0}^{\infty} q f_q(N_{ion}t_r, d_p). \quad (5)$$

Following the procedure described by Büscher et al. (1994), a value $N_{ion}t_r \approx 1 \times 10^{13}$ ions s m^{-3} was inferred from measurements of ϕ and the ion current passing across the flow conduit around the screen electrode inside a prototype monitor. At $N_{ion}t_r = 1 \times 10^{13}$ ions s m^{-3}, the Fuchs theory predicts the substantially linear relationship

$$Q(d_p) = 0.038 d_p \quad (6)$$

(d_p in units "nm") with a correlation coefficient $R^2 = 0.9998$. Deviations from linearity are predicted only for $d_p \leq 10$ nm for reasons that then just a fraction of the particles can still become charged with only a single ion. Leaving the latter complication aside, a substitution of Eq. 5 in Eq. 1 with $Q(d_p) \propto d_p$ yields

$$I_1 = C_1 \int_{d_p=0}^{\infty} d_p \frac{dN(d_p)}{d\ln(d_p)} d\ln(d_p)$$
$$= C_1 N d_{p,av} = C_1 L \quad (7)$$

wherein, $d_{p,av}$ is the number-averaged particle diameter defined according to

$$d_{p,av} = \frac{\int_{dp=0}^{\infty} d_p \frac{dN(d_p)}{d\ln(d_p)} d\ln(d_p)}{\int_{dp=0}^{\infty} \frac{dN(d_p)}{d\ln(d_p)} d\ln(d_p)} = \frac{L}{N}.$$

C_1 denotes a parameter whose magnitude depends on the process variables ϕ and $N_{ion}t_r$. These are normally held constant for a given monitor, thus making C_1 a constant proportionality factor. $L = Nd_{p,av}$ denotes the particle length concentration.

The outcome of Eq. 7 was verified by measuring I_1 as a function of $Nd_{p,av}$ for various aerosol size distributions and concentrations. For this purpose, aerosols were generated by atomizing dilute aqueous KNO_3 or NaCl salt solutions in a Condensation Aerosol Generator SLG 250 (Topas, Dresden, Germany) capable of emitting the salt nuclei either as produced or after size enlargement by contacting them with condensing DEHS vapor. The final size of the produced particles was adapted via controlled heating of the DEHS liquid in the SLG 250 which determined the DEHS vapor pressure in the condensation chamber. Values of $d_{p,av}$ could be obtained throughout the 20–130 nm size range (accounting for particles with diameters up to about 300 nm). Changes in N were realized by altering the airflow with which the aerosol particles were carried away from the aerosol generator toward the measuring chamber. Resulting values for N fell within the 10000–800000 part/cm^3 concentration range. A Scanning Mobility Particle Sizer (SMPS) instrument (Grimm Aerosol Technik, Germany) comprising a Differential Mobility Analyzer (DMA, Model #55–340) and a Condensation Particle Counter (CPC, Model #5403) was used as a reference instrument to independently measure the particle size distribution in the 6–340 nm size range. Values for both N and $d_{p,av}$ were independently obtained from the recorded particle size distribution for computing $L = Nd_{p,av}$.

Results for I_1 as a function of $L = Nd_{p,av}$ are shown in Fig. 2. They entirely confirm the prediction of Eq. 7 that $I_1 \propto L$. The average particle charge was found to be $Q(d_{p,av}) \approx 0.035 d_{p,av}$, in close agreement with Eq. 6.

Inferring the particle number concentration N

From the particle length concentration L, it is possible to infer an approximate "apparent" number concentration N_{app} according to

$$N_{app} = \frac{N \times d_{p,av}}{d^*_{p,av}} \quad (8)$$

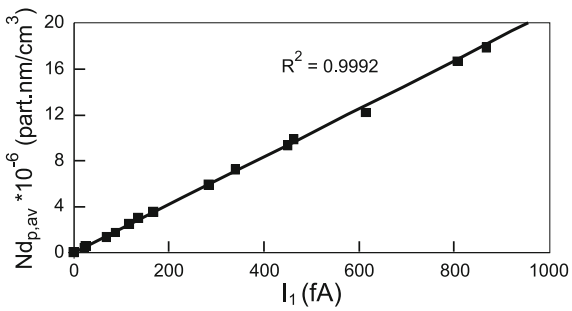

Fig. 2 The particle length concentration $L = Nd_{p,av}$ as a function of I_1

with $d^*_{p,av}$ denoting a default average particle diameter. As an example, measurements on combustion-related UFPs in outdoor air showed that $d_{p,av}$ typically falls within the 25–100 nm size range. Taking a default $d^*_{p,av} = 50$ nm, a measurement of I_1 becomes sufficient to infer a value for N_{app} that differs at most by a factor of 2 from N. As such

$$N_{app} = S_{N_{app}} I_1 \tag{9}$$

with $S_{N_{app}}$, a calibration factor. In the air of a given workplace environment, it is plausible that the encountered particle size distribution remains relatively constant over time. A reference instrument can then determine $d^*_{p,av} \approx d_{p,av}$ for that workplace to minimize the difference between N and N_{app}. Note that for inferring N_{app} from I_1 according to Eq. 9, it is sufficient to use the monitor depicted in Fig. 1 without the precipitation section.

It will now be shown how a more accurate value for N can be extracted from a measurement of the signal difference (I_1–I_2) under the condition that process conditions are chosen such that

$$\xi_q(d_p, E_{pl}) = \frac{qeC_c(d_p)E_{pl}L_{pl}}{3\pi\eta_{air}d_p v_{air}d_{pl}} < 1 \tag{10}$$

for all charged particles of diameter d_p that contribute to a non-negligible extent to N. From Eqs. 1, 3, and 4

$$\begin{aligned} I_1 - I_2 &= \int_{d_p=0}^{\infty} \sum_{q=0}^{\infty} qe\phi f_q(N_{ion}t_r, d_p)\xi_q(d_p) \\ &\quad \times \frac{dN(d_p)}{d\ln(d_p)} d\ln(d_p) \\ &= \int_{d_p=0}^{\infty} \sum_{q=0}^{\infty} qe\phi f_q(N_{ion}t_r, d_p)\frac{qeC_c(d_p)E_{pl}L_{pl}}{3\pi\eta_{air}d_p v_{air}d_{pl}} \\ &\quad \times \frac{dN(d_p)}{d\ln(d_p)} d\ln(d_p) \\ &\propto \int_{d_p=0}^{\infty} \sum_{q=0}^{\infty} q^2 f_q(N_{ion}t_r, d_p)\frac{C_c(d_p)}{d_p} \\ &\quad \times \frac{dN(d_p)}{d\ln(d_p)} d\ln(d_p) \\ &\propto \int_{d_p=0}^{\infty} Q^2(d_p)\frac{C_c(d_p)}{d_p} \times \frac{dN(d_p)}{d\ln(d_p)} d\ln(d_p). \end{aligned} \tag{11}$$

Using the result obtained from Eq. 6, wherein $Q(d_p) \propto d_p$ while $C_c(d_p) \propto 1/d_p$ for $d_p < 100$ nm, one arrives at

$$I_1 - I_2 \propto \int_{d_p=0}^{\infty} \frac{dN(d_p)}{d\ln(d_p)} d\ln(d_p) \propto N \tag{12}$$

Thus predicting a linear relationship between ($I_1 - I_2$) and N. More detailed information about the validity domain of the latter outcome at a given set of process conditions was theoretically obtained by investigating the constancy of the parameter A_0 in

$$A_0 = \frac{I_1 - I_2}{N} \tag{13}$$

as a function of $d_{p,av}$, E_{pl} and σ at $\frac{\phi L_{pl}}{v_{air} d_{pl}} = 6.9 \times 10^{-4}$ m^2 with $N_{ion}t_r = 1 \times 10^{13}$ ions s m^{-3} and $\phi = 0.53$ L/min. In practice, most UFP size distributions can be described in terms of a single or linear combination of several log-normal size distributions. A log-normal size distribution expressed in terms of N, $d_{p,av}$ and the size distribution parameter σ has the form

$$\begin{aligned} dN(d_p) &= \frac{N}{\sqrt{2\pi}\ln\sigma} \\ &\quad \times \exp\left[-\frac{\left(\ln d_p - \ln d_{p,av} + \frac{\ln^2\sigma}{2}\right)^2}{2(\ln\sigma)^2}\right] d\ln(d_p). \end{aligned} \tag{14}$$

Examples of a few log-normal size distributions at a constant $d_{p,av}$ but different values for σ are shown in Fig. 3. A narrow size distribution is obtained at $\sigma = 1.2$; a wide size distribution exists at $\sigma = 2.5$.

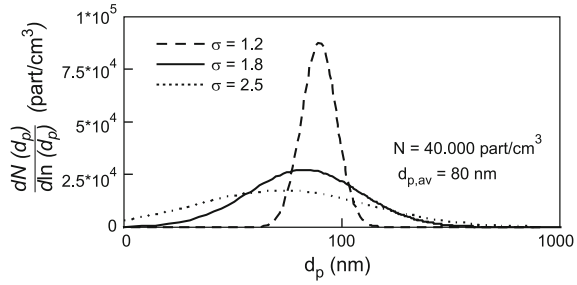

Fig. 3 Mono-modal log-normal particle size distributions at different values σ

Computed results for A_0 are shown in Fig. 4, which also gives the characteristic particle diameter d_0 at the used value for E_{pl}. For $d_p \leq d_0$ and $q \geq 1$, one has $\xi_q(d_p) = 1$, i.e., full precipitation of all charged particles. For $d_p > d_0$ and $q = 1$, only partial precipitation occurs with $\xi_1(d_p) < 1$. Provided that an error margin of up to 20% is allowed, Fig. 4 confirms that A_0 is relatively independent of both $d_{p,av}$ and σ, when conditions exist that only induce a partial precipitation of all charged particles with $d_p \geq 20$ nm. Favorable conditions exist in particular, when $E_{pl} = 25$ V/mm ($d_0 = 21$ nm) at which $A_0 \approx (1.10 \pm 0.15) \times 10^{-3}$ fA cm^3 throughout the range 20 nm $\leq d_{p,av} \leq$ 100 nm for $1.2 \leq \sigma \leq 2.5$. This covers most situations of practical interest. Deviations in the predicted A_0 value from constancy occur mostly in the range 20 nm $\leq d_{p,av} \leq 40$ at $\sigma > 2$. At the reduced $E_{pl} = 12.5$ V/mm ($d_0 = 15$ nm), A_0 becomes relatively more dependent on $d_{p,av}$ for $d_{p,av} \leq 30$ nm, when $\sigma \leq 1.8$. The reason lies in the then more pronounced effect of the particle charge distribution statistics. Reducing E_{pl} has the additional disadvantage that $(I_1 - I_2)$ becomes smaller and thus more difficult to be measured accurately. Increasing E_{pl} to $E_{pl} = 40$ V/mm leads to a disappearance of the constancy of A_0 across the size range 20 nm $\leq d_{p,av} \leq$ 120 nm, thereby much increasing the error, when N is to be inferred from the measured value $(I_1 - I_2)$ according to Eq. 13. In conclusion, the choice $E_{pl} \approx 25$ V/mm ($d_0 \approx 20$ nm) is preferred since it induces both a relative difference $(I_1 - I_2)$ that is sufficiently large to be properly measurable and which allows N to be inferred according to Eq. 13 within an estimated accuracy of ±20%.

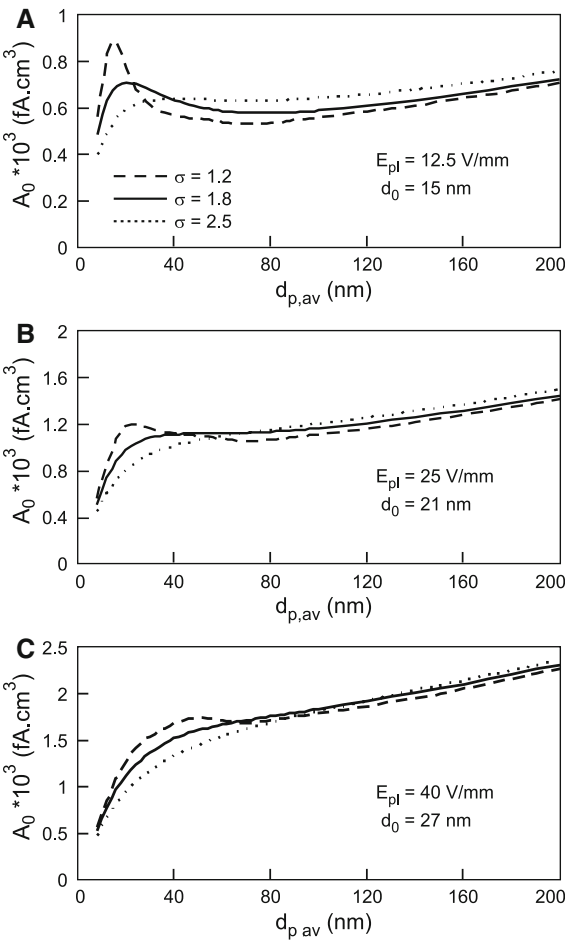

Fig. 4 Computations of A_0 as a function of $d_{p,av}$, σ, and E_{pl} for mono-modal log-normal particle size distributions

The above prediction was experimentally tested with an Aerasense NP monitor, wherein process conditions were enabled similar to those underlying the computations used for deriving the data in Fig. 4. The result is shown in Fig. 5, wherein N was varied over almost three orders of magnitude ($1000 < N < 800000$ part/cm^3). In parallel, values for σ were in the $\sigma = 1.2$–1.8 region, while $d_{p,av}$ varied from 20–125 nm. All data for N, $d_{p,av}$, and σ were obtained from parallel SMPS measurements. Figure 5 confirms a linear relationship according to

$$N = S_N(I_1 - I_2) \tag{15}$$

with a correlation coefficient $R^2 = 0.996$. This result is even better as what might be expected on the basis of the computational results shown in Fig. 4.

We note that a particle size distribution characterized with $d_{p,av} \approx 100$ nm at $\sigma > 1.2$ comprises particles with diameters up to about $d_p = 300$ nm (see e.g., the size distributions in Fig. 3). This confirms the

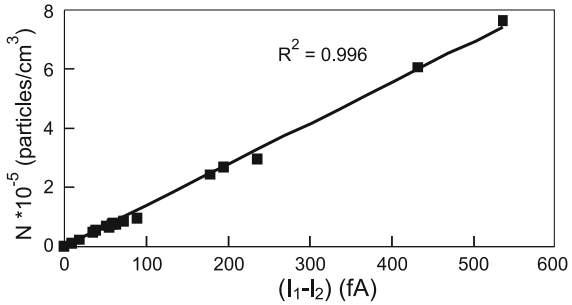

Fig. 5 Measured relationship between N and $(I_1 - I_2)$

suitability of the Aerasense NP monitor for detecting airborne particles in the 10–300 nm size range.

Inferring the average particle diameter $d_{p,av}$ when $d_{p,av} \leq 100$ nm

With the aforementioned results, it is possible to infer $d_{p,av}$ from L and N according to

$$d_{p,av} = \frac{L}{N} \propto \frac{I_1}{I_1 - I_2} \tag{16}$$

under the constraint that $d_{p,av} \leq 100$ nm. This is confirmed in Fig. 6, wherein $I_1/(I_1 - I_2)$ is plotted against $d_{p,av}$ at various N and σ values, as inferred from independent SMPS measurements. A linear relationship is apparent with a correlation coefficient $R^2 = 0.975$ according to

$$d_{p,av} = S_{dp}\frac{I_1}{I_1 - I_2} \tag{17}$$

up to $d_{p,av} \approx 100$ nm. Note that the scaling factor $S_{N_{app}}$ introduced in Eq. 9 relates to S_N and S_{dp} according to

$$S_{N_{app}} = \frac{S_N S_{dp}}{d^*_{p,av}} \tag{18}$$

Separate knowledge of $d_{p,av}$ and N gives better insight in the NP and/or UFP air pollution characteristics and its likely origin. Furthermore, as will be discussed below, it can be used to get information about the particle surface area that deposits inside the respiratory tract following particle inhalation.

Inferring N and $d_{p,av}$ when $d_{p,av} > 100$ nm

In most situations of practical interest, particles with $d_p < 100$–150 nm account for over 95% of the total particle number concentration. This is normally consistent with a $d_{p,av} < 100$ nm. It is nevertheless worthwhile to briefly explore the situation, wherein $d_{p,av} > 100$–120 nm. The computed results depicted in Fig. 4 show that then the approximately linear relationship

$$A_0 = C_2 + C_3 d_{p,av} \tag{19}$$

holds, wherein C_2 and C_3 are constants. In Fig. 4b and c, A_0 hardly depends on the particle size distribution at $d_{p,av} \geq 100$ nm, so the same is true for C_2 and C_3. According to Eq. 13, this leads to

$$I_1 - I_2 = N\left(C_2 + C_3 d_{p,av}\right). \tag{20}$$

Combining Eq. 20 with Eq. 7 yields

$$\frac{I_1}{I_1 - I_2} = \frac{C_1 d_{p,av}}{C_2 + C_3 d_{p,av}} \quad \text{for } d_{p,av} > 100 - 120 \text{ nm}. \tag{21}$$

Equation 21 allows $d_{p,av}$ to be inferred from the signals I_1 and I_2, when C_1, C_2, and C_3 are known either from a theoretical calculation or from a calibration with a reference instrument. Subsequently, N is obtained from either Eq. 7 or Eq. 20.

Since the use of the Aerasense NP monitor is mainly intended for detecting particles with $d_p < 300$ nm, we did not pursue the experimental confirmation of the validity and applicability of Eqs. 19–21. Importantly, Eq. 17 is valid when $d_{p,av} \leq 100$ nm, whereas Eq 21 applies to the less common situations wherein $d_{p,av} > 100$ nm. Whether or not $d_{p,av} \leq 100$ nm becomes immediately evident from a substitution of I_1 and I_2 in Eq. 17, thereby making clear whether either Eq. 17 or Eq. 21 should be used for obtaining $d_{p,av}$. From Fig. 4c and b, it is furthermore evident that for $d_{p,av} > 100$ nm, a relatively more accurate determination of $d_{p,av}$ becomes possible when the precipitation section is operated at a field strength $E_{pl} \geq 25$ V/mm such that the factors C_2 and $C_3 d_{p,av}$ in Eq. 21 remain comparable in magnitude.

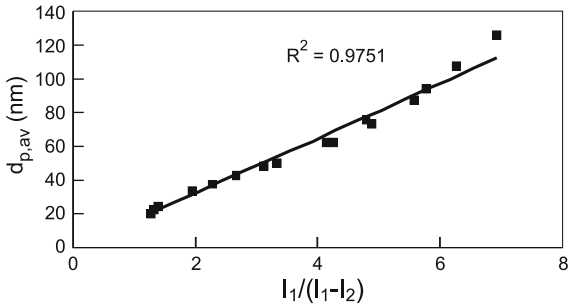

Fig. 6 Measured relationship between $d_{p,av}$ and $I_1/(I_1 - I_2)$

Inferring the inhalation-induced particle surface area deposition S

As mentioned before, inhaled non-soluble solid NPs may induce adverse health effects at the point of deposition in the respiratory tract or after transmission to other body organs. Toxicologists consider the

particle surface area as one relevant exposure measure because many processes in the body environment take place via the particle surface. The surface area strongly increases per unit particle mass when the particle size decreases (Oberdörster 1996; Donaldson et al. 1998). NP deposition in the tracheobronchial lung region (TB) as well as the alveolar lung region (AL) is potentially hazardous because of slow particle clearing mechanisms and the possible transfer of NPs into the blood with resulting distribution in several body organs. NP transfer into the blood is most likely to occur from the alveolar region. In the head airways (HA), NP transfer may occur from the nose via the olfactory nerve to the brain.

Figure 7 shows the fractional deposition efficiency curves of particles in various respiratory tract regions as a function of d_p. The data are obtained from ICRP Publication 66 (ICRP 1994) which relates to a nose-breathing reference worker under a set of specified breathing conditions (3,301 cm^3 functional residual lung capacity, 20 breaths per minute, 1.5 m^3/h ventilation rate, light exercise). The precise shape of the deposition efficiency curves is known to differ from person to person depending on gender, activity level, age, and the possible presence of respiratory ailments. The following discussion applies to the reference worker only, but can analogously be carried out for others when the particle deposition efficiencies in their respective lung compartments are known.

Analytical equations for the fractional deposition efficiencies $D_{HA}(d_p)$, $D_{TB}(d_p)$ and $D_{AL}(d_p)$ in the head airways, the tracheo-bronchial lung region and the alveolar lung region, respectively, have been reported in the literature (Hinds 1999) and will not be repeated here. At $d_p < 300$ nm, particle deposition in the lung is predominantly governed by diffusion. The diameter d_p in $D_{HA}(d_p)$, $D_{TB}(d_p)$, and $D_{AL}(d_p)$ is therefore the geometric diameter governing particle diffusion behavior. According to Sinclair et al. (1976), the mobility diameter governing the particle charging behavior is virtually identical to the geometric diameter and can therefore also be used for estimating the deposition efficiencies of these UFPs. The deposited particle surfaces areas S_{HA}, S_{TB}, and S_{AL} per unit volume of inhaled air comprising spherical particles follow from

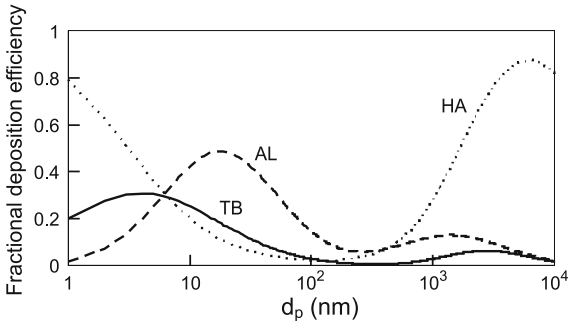

Fig. 7 Fractional deposition efficiency of inhaled particles in various lung compartments for a reference worker according to the ICRP model (ICRP 1994)

$$S_{HA} = \int_{dp=0}^{\infty} \pi d_p^2 D_{HA}(d_p) \frac{dN}{d\ln(d_p)} d\ln(d_p), \quad (22)$$

$$S_{TB} = \int_{dp=0}^{\infty} \pi d_p^2 D_{TB}(d_p) \frac{dN}{d\ln(d_p)} d\ln(d_p), \quad (23)$$

$$S_{AL} = \int_{dp=0}^{\infty} \pi d_p^2 D_{AL}(d_p) \frac{dN}{d\ln(d_p)} d\ln(d_p). \quad (24)$$

The log-normal size distribution in Eq. 14 is an example of a possible particle size distribution $\frac{dN}{d\ln(d_p)}$. Most size distributions encountered in practice can be represented by a linear combination of 2 or 3 log-normal particle size distributions.

Examples of computations of S as a function of $d_{p,av}$ and σ according to Eqs. 22–24 are shown in Fig. 8 with an arbitrary-chosen $N = 100{,}000$ part/cm^3. Remarkably, the results for S_{TB} and S_{AL} are rather independent of σ across the broad range $1.2 \le \sigma \le 2.4$ up to $d_{p,av} = 100$ nm, covering many practical situations of interest. Within an error of 10–20%, both S_{TB} and S_{AL} can be expressed as a function of $d_{p,av}$ and N only, provided that $d_{p,av} < 80$–100 nm. With N and $d_{p,av}$ obtained from I_1 and I_2, this result also allows S_{TB} and S_{AL} to be directly inferred, at least for the reference worker under consideration.

A quick computation of $S_{TB}(N, d_{p,av})$ and $S_{AL}(N, d_{p,av})$ can be done by making use of the following expressions for the fitted solid curves in Fig. 8

$$S_{TB}(N, d_{p,av}) = 10^{-6} N \left(4 d_{p,av}^{1.33} - 1.05 \times 10^{-2} d_{p,av}^{2.6} + 6.4 \times 10^{-5} d_{p,av}^{3.52} - 5.2 \times 10^{-10} d_{p,av}^{5.4}\right)$$
$$S_{AL}(N, d_{p,av}) = 10^{-5} N \left(5.4 d_{p,av} - 38\right) \quad (25)$$

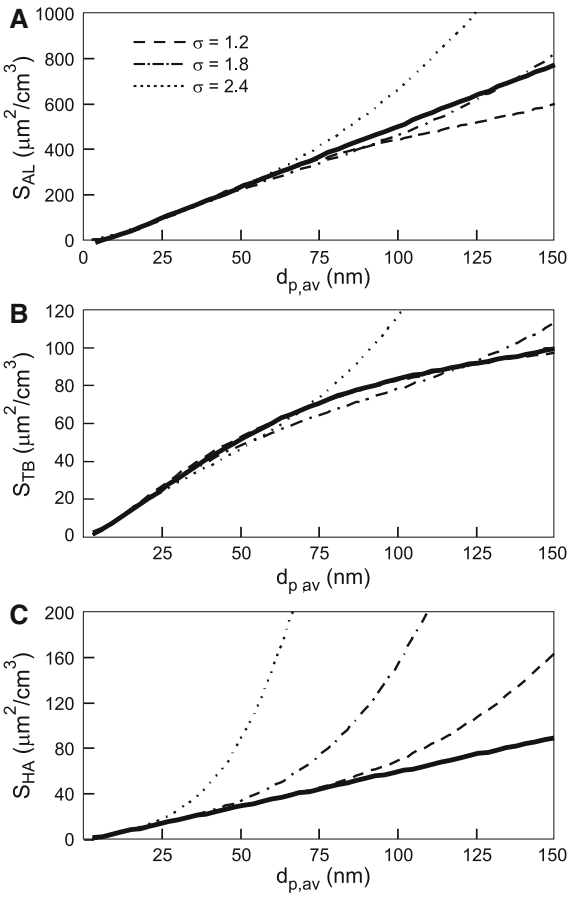

Fig. 8 Predicted surface area concentrations S that deposit in the AL, TB and HA regions of the lung, respectively, as a function of $d_{p,av}$ and σ at $N = 100{,}000$ part/cm^3 for a reference worker inhaling these particles. Solid lines represent the analytical approximations according to Eq. 25

wherein N must be substituted in part/cm^3, and $d_{p,av}$ in "nm", yielding S_{TB} and S_{AL} in μm^2/cm^3. The validity of Eq. 25 is limited to spherical particles with $d_{p,av} < 80$–100 nm when also a wide particle size distribution with $\sigma \approx 2.4$ is to be properly accounted for. However, this size range is sufficiently wide to account for NP exposure and accounts for airborne particles with sizes up to $d_p = 300$–400 nm. It is furthermore assumed that the $d_{p,av}$ of inhaled particles does not change through moisture uptake during inhalation. This limits the applicability of the present discussion to solid non-hygroscopic particles. Irregular-shaped particle agglomerates cannot be accounted for.

Computed results for S_{HA} shown in Fig. 8c markedly depend on σ. Without upfront knowledge about the characteristics of the particle size distribution, it appears at first sight not possible to infer S_{HA} from N and $d_{p,av}$ only. However, inspection of the HA deposition efficiency curve in Fig. 7 reveals that the upswing in the curves for S_{HA} in Fig. 8 can be ascribed to the deposition of larger particles with $d_p > 100$ nm. These larger particles are less likely to be transferable from the nose to the brain. Considering only the deposited surface area S_{HA} of inhaled NPs with $d_p < 100$ nm, the solid straight line drawn in the S_{HA} diagram of Fig. 8c can be used to account for their deposition.

Without losing much accuracy, the solid lines drawn in Fig. 8 for S_{AL} and S_{TB} can also be approximated as linear functions of the product $Nd_{p,av}$ for $25 \le d_{p,av} \le 80$ nm according to

$$S_{AL}(N, d_{p,av}) \approx 4.7 \times 10^{-5} N d_{p,av} \approx C_{AL} I_1 \quad (26)$$

$$S_{TB}(N, d_{p,av}) \approx 0.95 \times 10^{-5} N d_{p,av} \approx 0.20 C_{AL} I_1 \quad (27)$$

$$S_{HA}(N, d_{p,av}) \approx 0.6 \times 10^{-5} N d_{p,av} \approx 0.13 C_{AL} I_1 \quad (28)$$

with N expressed in part/cm^3 and $d_{p,av}$ in "nm", yielding S in μm^2/cm^3. These functions are re-drawn in Fig. 9. The constant C_{AL} follows from the relationship between I_1 and $Nd_{p,av}$ (see Fig. 2). Equations 26–28 predict I_1 to represent a key signal that is proportional to the NP exposure concerning the deposited surface area concentrations of inhaled NPs inside the respiratory tract. Use of the NP monitor shown in Fig. 1 without the precipitation section is sufficient for this measurement and it is not necessary to independently obtain values for N and $d_{p,av}$.

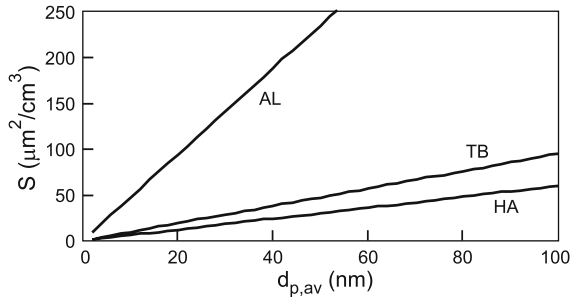

Fig. 9 S_{AL}, S_{TB}, and S_{HA} as a function of $d_{p,av}$ at $N = 100{,}000$ part/cm^3 for a reference worker inhaling these particles according to Eqs. 26–28

Based on the above results, the Aerasense NP monitor is enabled to provide a pollution index number P whose numerical value relates to the relative risk associated with NP exposure according to

$$P = C_P \log\left(\frac{Nd_{p,av}}{(Nd_{p,av})_0}\right) \quad \text{for } Nd_{p,av} \geq (Nd_{p,av})_0$$
$$P = 0 \quad \text{for } Nd_{p,av} < (Nd_{p,av})_0 \tag{29}$$

C_P is an arbitrary proportionality constant. The length concentration $(Nd_{p,av})_0$ denotes the safe concentration threshold below which the risk associated with NP exposure is considered to be negligible. A higher NP toxicity is to be accounted for by setting $(Nd_{p,av})_0$ at a lower value. Expressing the exposure-associated risk via a single numerical value for P can be advantageous for communication purposes.

Apart from the product $Nd_{p,av}$, independent knowledge about N and $d_{p,av}$ as well as the chemical properties and agglomeration state of the particles remains desirable to better understand the nature, characteristics, and toxicology of particulate air pollution with NPs.

The measuring sensitivity of the Aerasense NP monitor

A desirable requirement for a personal NP monitor is that it can be embodied as a light-weight low-noise portable instrument equipped with a rechargeable battery and a data logger. This demands size minimization of the hardware, however size reduction unavoidably reduces the measuring sensitivity. A first reason for this limitation is that electronic noise limits the accuracy of currently available operational amplifiers to 1 fA at best. A second reason is that $I_{sensor} \propto \phi$ (see Eq. 1), but the attainable airflow ϕ through the monitor is constrained by hardware size and the allowed power consumption and noise levels. An increased measuring sensitivity can therefore not be attained without increasing the size of the device. Another circumstance affecting the monitor's sensitivity/accuracy is that the separate determination of N and $d_{p,av}$ relies on a serial measurement of two sensor signals I_1 and I_2. Considering the case wherein $d_{p,av} \leq 100$ nm, I_1 and I_2 can be substituted in Eqs. 15 and 17 only when the NP pollution characteristics (in terms of N and $d_{p,av}$) remain constant during the time interval wherein both I_1 and I_2 are recorded. When this is not the case, an error will be made which becomes worse when the rate of change in the NP pollution characteristics increases. In what follows, we will consider the NP monitor's sensitivity under both static conditions and transient conditions in time with respect to the NP pollution characteristics.

Static NP pollution characteristics

Our research revealed that a truly portable monitor can only be realized at $\phi \leq 0.5$ L/min. A table-top device results when $\phi \geq 1$ L/min is needed. Within certain limits, the device size roughly scales with ϕ by increasing its cross-section in the direction perpendicular to the airflow such as to ensure the air velocities inside the device to remain constant and independent of ϕ. This approach also enables the device to be operated at near constant power and noise levels.

Assuming Eqs. 15 and 17 to be valid, it is worthwhile to discuss the monitor's sensitivity limits under some practical conditions. At a constant $N_{ion}t_r$, it follows from the Fuchs theory and Eqs. 1, 9, 15, and 17 that at an airflow ϕ relative to a reference airflow ϕ^*,

$$N = S_N \frac{\phi^*}{\phi}(I_1 - I_2) \tag{30}$$

$$N_{app} = S_{N_{app}} \frac{\phi^*}{\phi} I_1 = \frac{S_N S_{dp}}{d^*_{p,av}} \frac{\phi^*}{\phi} I_1 \tag{31}$$

$$d_{p,av} = S_{dp} \frac{I_1}{I_1 - I_2} \tag{32}$$

$$Nd_{p,av} = S_N S_{dp} \frac{\phi^*}{\phi} I_1. \tag{33}$$

The inaccuracies in deducing N, N_{app}, and $d_{p,av}$ from the sensor signals relate to the inaccuracy ΔI in I_1 and I_2 according to

$$\frac{\Delta N}{N} = \frac{2S_N}{N} \frac{\phi^*}{\phi} \Delta I \tag{34}$$

$$\frac{\Delta N_{app}}{N_{app}} = \frac{S_N S_{dp}}{N_{app} d^*_{p,av}} \frac{\phi^*}{\phi} \Delta I \tag{35}$$

$$\frac{\Delta d_{\mathrm{p,av}}}{d_{\mathrm{p,av}}} = \frac{\Delta I}{I_1} + \frac{2\Delta I}{I_1 - I_2} \tag{36}$$

$$= \frac{\phi^*}{\phi}\frac{\Delta I}{N}\left(\frac{S_{\mathrm{N}} S_{\mathrm{dp}}}{d_{\mathrm{p,av}}} + 2S_N\right). \tag{37}$$

Equations 34–37 confirm the improving accuracy of the inferred N and $d_{\mathrm{p,av}}$ at increasing ϕ and/or N. Specifically, at constant parameters $N_{\mathrm{ion}} t_{\mathrm{r}} = 1 \times 10^{13}$ ions s m^{-3}, $\phi^* = 0.53$ L/min (about the limit of portability), $d^*_{\mathrm{p,av}} = 50$ nm, $E_{\mathrm{pl}} = 25$ V/mm, and $\frac{\phi^* E_{\mathrm{pl}} L_{\mathrm{pl}}}{\mathrm{V}_{\mathrm{air}} d_{\mathrm{pl}}} = 17.25$ Vm, one has $S_{\mathrm{dp}} = 20.2$ nm and $S_{\mathrm{N}} = 900$ part cm^{-3} fA^{-1}. This results in

$$\frac{\Delta N}{N} \approx \frac{1800}{N}\frac{\phi^*}{\phi}\Delta I \tag{38}$$

$$\frac{\Delta N_{\mathrm{app}}}{N_{\mathrm{app}}} \approx \frac{360}{N_{\mathrm{app}}}\frac{\phi^*}{\phi}\Delta I \tag{39}$$

$$\frac{\Delta d_{\mathrm{p,av}}}{d_{\mathrm{p,av}}} \approx \frac{\phi^*}{\phi}\frac{\Delta \mathrm{I}}{N}\left(\frac{18200}{d_{\mathrm{p,av}}} + 1800\right). \tag{40}$$

According to Eq. 38, $\Delta N \approx 1800$ part/cm^3 at $\Delta I = 1$ fA for a single measurement at $\phi = \phi^*$. The latter ΔN value may be compared with ambient NP concentration values in "clean" outdoor air, wherein $N \leq 10.000$ part/cm^3, and in "slightly polluted" outdoor air wherein $10.000 \leq N \leq 30.000$ part/cm^3. Averaging successively obtained values for N over a period of time can much reduce ΔN, but only so when the air pollution characteristics remain substantially constant over this period. At $N = 10{,}000$ part/cm^3 and $d_{\mathrm{p,av}} = 50$ nm, Eq. 40 predicts $\Delta d_{\mathrm{p,av}} \approx 11$ nm when $\Delta I = 1$ fA.

An improved measuring accuracy is attained by reducing ΔI to below 1 fA. This is accomplished in the Aerasense NP monitor by incorporating an advanced signal filtering procedure for the sensor signal I_{sensor} together with an averaging procedure of sampled filtered signals I_{sensor} for a finite period of time, leading to $\Delta I \approx 0.2$–0.4 fA. The latter reduction of ΔI reduces the inaccuracy in N down to $\Delta N \approx 500$–700 part/cm^3.

Comparing Eq. 38 with 39 shows that $\Delta N_{\mathrm{app}} < \Delta N$, obviously because N_{app} is directly inferred from only a single sensor signal. Assuming the health risk associated with NP exposure to be proportional to the deposited surface areas S according to Eqs. 26–28, the relative uncertainty $\frac{\Delta S}{S}$ with respect to this risk follows from

$$\frac{\Delta S}{S} = \frac{\Delta I}{I_1} = \frac{\Delta N_{\mathrm{app}}}{N_{\mathrm{app}}} \approx \frac{360}{N_{\mathrm{app}}}\frac{\phi^*}{\phi}\Delta I. \tag{41}$$

From Eqs. 38 and 41, $\frac{\Delta S}{S} = 0.2\frac{\Delta N}{N}$ i.e., S is measured more accurately than N.

Thus, a characterization of the NP air pollution characteristics in terms of N and $\mathrm{d}_{\mathrm{p,av}}$ under static conditions is possible with a portable NP monitor at $\phi = \phi^* \approx 0.5$ L/min with $\Delta N \approx 500$–700 part/cm^3 and $\Delta d_{\mathrm{p,av}} \approx 3$–$4$ nm. This result is to be compared with the outcome of the earlier discussion on the results in Fig. 4, which led to the conclusion that the validity of Eq. 15 is subject to a $\pm 20\%$ uncertainty range. The latter percentage remains therefore the dominating contribution to the overall uncertainty in the inferred value for N and this intrinsic uncertainty cannot be diminished via changes in ϕ and/or E_{pl}. The same applies to the inferred value for $d_{\mathrm{p,av}}$. Clearly, the relative exposure risk obtained from the measured $Nd_{\mathrm{p,av}} \propto \mathrm{I}_1$ can always be inferred more accurately than the individual values for N and $d_{\mathrm{p,av}}$.

Transient NP pollution characteristics

In case the NP pollution characteristics change during the time period wherein I_1 and I_2 are serially measured, additional inaccuracy is incurred in the inferred NP pollution parameters because the validity of Eqs. 15 and 17 are compromised. Fast changes may even lead to recordings wherein $I_1 < I_2$, yielding non-physical negative values for N and $d_{\mathrm{p,av}}$. Parallel measurements of I_1 and I_2 rigorously solve this problem, but was not implemented in order to avoid the increasing system complexity. Note that the presence of pollution transients does not in any way affect the accuracy of the inferred risk-relevant values of S or P, because these only depend on the product $Nd_{\mathrm{p,av}} = Nd^*_{\mathrm{p,av}}$ which follows directly from I_1 according to Eq. 9 without a need to invoke I_2.

The Aerasense NP monitor incorporates an algorithm wherein serially measured signals I_1 and I_2 are used as input parameters to infer values for N and $d_{\mathrm{p,av}}$ that make physical sense also under highly transient conditions. One characteristic of this algorithm is that under transient conditions, change of the inferred $d_{\mathrm{p,av}}$ within the time period between two

successive measurements is allowed for but the extent of change is bounded by a set maximum value. No limitations are imposed with respect to changes in N. This approach makes physical sense because the relative change in $d_{p,av}$ within a brief period of time is normally much less than the relative change in N. This can still be checked afterwards when all inferred data for N and $d_{p,av}$ over the duration of the experiment are visualized on a computer screen. Another characteristic of this algorithm is that N and $d_{p,av}$ are inferred at each moment in time when either a new measurement of I_1 or of I_2 is recorded. The determinations of N and $d_{p,av}$ only involve the two most recently measured I_1 and I_2 values and the previously inferred value for $d_{p,av}$. In case $I_1 \leq I_2$ or when $I_1 \leq I_{min}$, with $I_{min,}$ a predefined minimum signal value, $d_{p,av}$ is left unchanged. In case the apparent relative change in $d_{p,av}$ remains within the predefined range, use is again made of Eq. 17 for the static situation. This procedure removes much scatter from the series of inferred data for $d_{p,av}$ over time without imposing restrictions on the rate of change in N. The product $Nd_{p,av}$, and therewith the inferred values for S and P according to Eqs. 26–29, still correspond with only the most recently measured value for I_1 just as under static NP pollution conditions.

Maintenance of the Aerasense NP monitor

Maintenance of the NP monitor involves periodic cleanings of the monitor's interior to ensure a constant airflow ϕ through the monitor and an undisturbed internal corona discharge for particle charging. Indeed, all airborne particulates entering the monitor will remain trapped therein, most of them in the filter disposed inside the Faraday cage. Because a virtually maintenance-free NP monitor is desirable, the following measures were taken for this purpose

- The inlet and sampling tube of the monitor are designed such that all airborne particles with $d_p \geq 10$ μm will have settled from the airflow before being able to reach the charging section of the monitor. These coarse settled particles can occasionally be easily removed from the tubing.
- The airflow ϕ through the monitor is limited at $\phi < 0.5$ L/min. Even at a fairly high constant airborne particle mass concentration of 50 μg/m^3, this will lead to a particle deposition of only 10 mg inside the monitor after 1 year of continuous operation. Initial experiments revealed that this small amount does not noticeably impede the monitor's functionality.
- Long-term exposure of the NP monitor to high particulate pollution levels is avoided by programming the NP monitor to operate only intermittently according to a duty cycle when the measured NP pollution level exceeds a set maximum concentration level. This significantly reduces the internal soiling of the monitor. Monitor operation according to a duty cycle can also be applied at more moderate pollution levels.
- The used ventilator atop the monitor in Fig. 1 has a rated lifetime of 4–5 years non-stop operation.

Based on the above implemented measures, it is foreseen that NP monitor servicing should be necessary only once in about 4 years. This servicing involves an internal cleaning of the monitor, a replacement of the filter inside the Faraday cage, a replacement of the ventilator, and a recalibration of the monitor's performance with respect to a benchmark NP monitor. It remains to be proven whether this predicted servicing frequency is sufficient for guaranteeing reliable monitor operation in the wide variety of practically encountered environments.

Benchmarking the Aerasense NP monitor

Several other types of NP monitors are commercially available that enable exposure measurements with respect to airborne NPs and UFPs. A widely used analytical instrument is the Scanning Mobility Particle Sizer (SMPS) which comprises a Differential Mobility Analyzer (DMA) and a Condensation Particle Counter (CPC). The SMPS is capable of measuring the UFP particle size distribution $\frac{dN(d_p)}{d\ln(d_p)}$ for particle sizes below $d_p = 1000$ nm, the most advanced ones down to $d_p = 2.5$ nm. Exposure-relevant information can be directly inferred from the measured particle size distribution. A SMPS is the instrument of choice for measuring particle size distribution details and for calibrating the Aerasense NP monitor. On the other hand, the SMPS is complex, bulky, and expensive, must be operated by a skilled person, and requires periodic maintenance.

Single (portable) CPC monitors are becoming popular for NP and UFP (source) detection. The CPC functionality is limited to measuring N with respect to all airborne particles larger than 3–10 nm. They cannot provide information about particle size or about inhalation-induced particle surface area deposition in the respiratory tract. A CPC is most accurate when $N < 10{,}000$ part/cm^3 because this allows the CPC to operate in the counting mode. For $N > 20{,}000$ part/cm^3, which is normal in many workplace environments, the CPC operates in photometric mode wherein individual particles cannot anymore be distinguished. Conversion of photometric signals into particle number concentrations relies on the use of calibration factors, however these appear to be rather sensitive to various instrumental and process parameters including the internal temperature settings. The authors found that at $N \geq 100.000$ part/cm^3, values for N determined with the CPC and with the SMPS, respectively, can differ by up to a factor a 2 whereas they substantially coincide when $N < 10.000$ part/cm^3. The CPC is less suited for uninterrupted continuous use and requires periodic refilling of its liquid reservoir. The handling of all types of CPCs requires due care because spillage of the liquid from its reservoir disables the instrument operation.

Based on an existing Electrical Aerosol Detector (EAD, TSI Model 3070), TSI recently introduced the Nanoparticle Surface Area Monitor (NSAM) capable of inferring the particle surface areas per unit volume of inhaled air that deposit in the AL and TB lung regions (Shin et al. 2007). The NSAM incorporates diffusion charging (albeit with a different charging process than in the Aerasense NP monitor) resulting in a particle charge $Q(d_p) = 0.021 \times d_p^{1.13}$ on monodisperse particles smaller than 100 nm. This is similar to the value $Q(d_p) \approx 0.035 \times d_{p,av}$ achieved in the Aerasense monitor. By varying the voltage on an internal ion trap, the NSAM output signals are made to correspond with the surface area concentrations of inhaled particles with $d_p < 100$ nm that deposit in the AL and TB lung regions. This procedure is different than described above for the Aerasense monitor, but the final results are comparable. In this regard, the functionality of the NSAM parallels that of the Aerasense monitor, however the NSAM does not provide information about N and/or $d_{p,av}$.

Another monitor incorporating diffusion charging is the LQ1-DC monitor (Matter Engineering) which reportedly charges particles according to $Q(d_p) = 0.0028 \times d_p^{1.36}$ (Jung and Kittelson 2005). The latter charge level is well below the $Q(d_p) \approx 0.035 \times d_p$ encountered in the Aerasense monitor and makes the LQ1-DC a relatively less sensitive device. The larger exponent of d_p is used to relate the LQ1-DC output signal to the active surface area (or Fuchs' surface area) of particles available for interaction with airborne ions. However, because of incomplete NP deposition in the respiratory system, only part of this "active surface area" relates to the health effects of inhaled NPs. The LQ1-DC cannot provide information about N and/or $d_{p,av}$.

The DC2000CE (Ecochem Analytics) diffusion charger appears similar to the LQ1-DC monitor, yielding a signal from which the active surface area can be inferred. The instrument specifications mention that the correlation between the active surface area and the output signal is site specific and must be re-calibrated with the help of a SMPS instrument when the site of measurement is changed.

The Aerasense NP monitor in a workplace environment

An Aerasense NP monitor was used for uninterrupted periods of at least several hours in two different workplaces that were both ventilated with filtered outdoor air.

In the first workplace, an extrusion process was carried out that involved the compounding of NPs in an organic matrix. Chemical analysis of sampled airborne particles indicated that virtually no engineered NPs contributed to the encountered NP pollution and that the measured NP pollution comprised only ambient particles derived from other sources. Values for N_{app} were continuously recorded with an Aerasense NP monitor that did not have a precipitation section. Results were compared with values for N and $d_{p,av}$ measured with a SMPS instrument (Type #5403; Grimm, Germany) capable of measuring the particle size distribution in 44 size channels in the 11 nm $\leq d_p \leq$ 1083 nm particle size interval. Figure 10 presents data for N_{app} and N. Observed values for N are about 25% less than those for N_{app}, however this can be partly explained by the circumstance that the actual $d_{p,av}$ was in the 54–58 nm range, as obtained from the SMPS results,

whereas the NP monitor used a default $d^*_{p,av} = 50$ nm, resulting in a value for N_{app} that is 10–15% too high (see Eq. 8). In addition, a small part of the NP monitor signal comes from particles with $d_p \leq 10$ nm, while the SMPS only counts particles with $d_p \geq 11$ nm. Apart from that, the agreement is satisfactory. A noteworthy feature is that the NP monitor measures at a rate of 0.1 Hz whereas the SMPS requires almost 7 min for each full scan. The extra time-resolved power of the NP monitor, which can be further increased up to 0.3 Hz, is advantageous for detecting rapidly passing transient peaks in the air pollution level that may accompany certain events.

In the second workplace, a NP manufacturing process was carried out in a closed chemical reactor vessel. It was discovered during process operation that the presence of several red-hot heated surfaces exposed to air acted as a major NP source creating a relatively high NP pollution level comprising NPs of unknown toxicity. Incidental welding activities in the workplace further contributed to the NP pollution creating transient high pollution peaks. Manufactured NPs could not be detected on the surfaces of any of the used air sampling filters. Figure 11 presents a series of data for N measured with the NP monitor and the SMPS between 19.45 p.m. until the next morning at 8.45 a.m. During this period, NP concentration differences of almost two orders of magnitude were encountered. Figure 12 presents simultaneously measured values for $d_{p,av}$ during the same time interval. Agreement between the NP monitor data and the SMPS data is very good. Again, it is clear from the presented data that transient peaks in the air pollution level can be easily detected by the NP monitor whereas they can remain invisible for the SMPS.

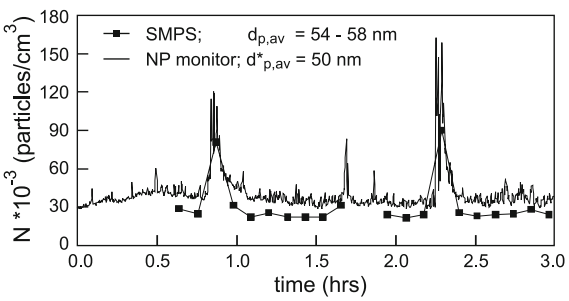

Fig. 10 N_{app} and N measured with the Aerasense NP monitor and with the SMPS, respectively

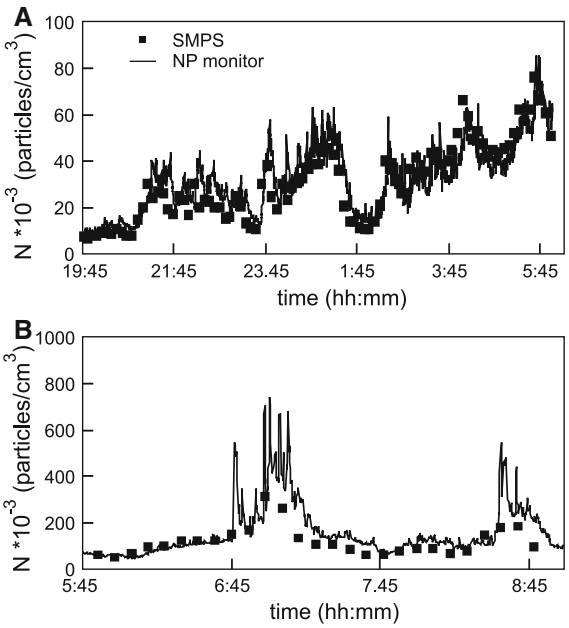

Fig. 11 N measured with the Aerasense NP monitor and with the SMPS

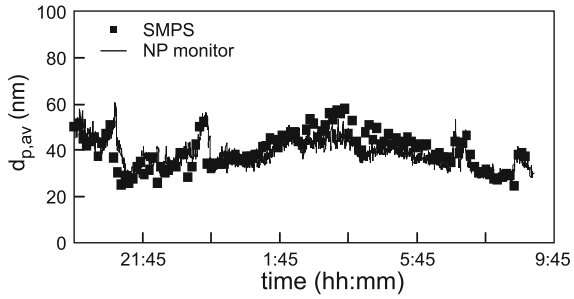

Fig. 12 $d_{p,av}$ measured with the Aerasense NP monitor and with the SMPS

Conclusions

The Aerasense NP monitor is a low-maintenance device for characterizing the NP air pollution in terms of N and $d_{p,av}$. Further to that, it can assess the relative health risk of inhaled NPs through the direct determination of the particle length concentration $L = Nd_{p,av}$ as a single concentration metric. L is linearly proportional to I_1 and comprises information about both particle number concentration and particle size. For the reference worker considered by the ICRP (1994), knowledge of L is sufficient to approximately determine the NP surface areas per unit volume of

inhaled air that deposit in the AL, TB and HA sections of the respiratory tract, respectively. A measurement of L can be done up to a frequency of 0.3 Hz. Inferring separate values for N and $d_{p,av}$ from the sensor signals is possible up to a frequency of 0.1 Hz. These frequencies allow relatively fast measurements to be carried out in workplace environments, whereby transient peaks in the NP pollution level can be detected at a much higher resolving power than what is possible with a SMPS.

Up to a certain measuring sensitivity, the NP monitor can be embodied as a portable battery-powered instrument that allows a direct sampling of the air during a work shift from the immediate breathing zone of a worker. This enables personal NP exposure assessments to be carried out at any moment. A determination of the integrated exposure during a period of time is obtained by integrating the measurement signals over time. At a given constant NP pollution level, the measuring sensitivity of the Aerasense NP monitor can be improved by increasing the sampled airflow ϕ through the sensor. This must preferably be done in parallel with a proportional increase in the sensor size such as to maintain constant airflow speeds inside the sensor independent of ϕ.

Complete risk assessment involves not only exposure assessment but also knowledge about the toxicity of the NPs. Furthermore, when the (suspected) toxicity of the NPs released in air at the workplace differs from that of the ambient NPs produced by other sources (e.g., from outdoor air pollution), it is necessary to first remove the ambient NPs from the ventilation air before an assessment of exposure and risk concerning the workplace-generated NPs can be carried out.

Other than for personal exposure assessment, the Aerasense NP monitor can be used for a wide range of other purposes such as:

- checking the efficiency of installed air filtration units,
- enabling automatic feedback to air handling and air cleaning units,
- realizing early warning systems,
- monitoring the ambient NP and UFP air pollution level, both indoor and outdoor.

Last but not least, use of the Aerasense monitor can help to create a better awareness about air pollution with NPs and its potential health risk.

References

Adachi M, Kousaka Y, Okuyama K (1985) Unipolar and bipolar diffusion charging of ultrafine aerosol particles. J Aerosol Sci 16(2):109–123

Büscher P, Schmidt-Ott A, Wiedensohler A (1994). Performance of a unipolar "square wave" diffusion charger with variable nt-product. J Aerosol Sci 25(4):651–663

Balbus JM, Florini K, Denison RA, Walsh SA (2007) Protecting workers and the environment: an environmental NGO's perspective on nanotechnology. J Nanopart Res 9(1):11–22

ICRP (1994) International Commission on Radiological Protection, Publication 66, Human Respiratory Tract Model for Radiological Protection. Elsevier Science Ltd, Oxford, Pergamon

Donaldson K, Li XY, MacNee W (1998) Ultrafine (nanometer) particle mediated lung injury. J Aerosol Sci 29(5–6):553–560

Elder A, Gelein R, Silva V, Feikert T, Opanashuk L, Carter J, Potter R, Maynard A, Ito Y, Finkelstein J, Oberdörster G (2006). Translocation of inhaled ultrafine manganese oxide particles to the central nervous system. Environ Health Perspect 114(8):1172–1178

Fissan H, Neumann S, Trampe A, Pui DYH, Shin WG (2007) Rationale and principle of an instrument measuring lung deposited nanoparticle surface area. J Nanopart Res 9(1):53–59

Geiser M, Rothen-Rutishauser B, Kapp N, Schurch S, Kreyling W, Schultz H, Semmler M, Hof VI, Heyder J, Gehr P (2005) Ultrafine particles cross cellular membranes by non-phagocytic mechanisms in lungs and in cultured cells. Environ Health Perspect 113:1555–1560

Hinds WC (1999) Aerosol technology: properties, behavior, and measurement of airborne particles, 2nd edn. Wiley, New York

Jung H, Kittelson DB (2005) Characterization of aerosol surface instruments in the transition regime. Aerosol Sci Technol 39:902–911

Kim JS, Yoon TJ, Yu KN, Kim BG, Park SJ, Kim HW, Lee KH, Park SB, Lee JK, Cho MH (2006) Toxicity and tissue distribution of magnetic nanoparticles in mice. Toxicol Sci 89(1):338–347

Kreyling WG, Semmler M, Erbe F, Mayer P, Takenaka S, Schultz H, Oberdörster G, Ziesenis A (2002) Translocation of ultrafine insoluble iridium particles from lung epithelium to extra-pulmonary organs is size dependent but very low. J Toxicol Environ Health A 65(20):1513–1530

Oberdörster G (1996) Significance of particle parameters in the evaluation of exposure dose-response relationships of inhaled particles. Part Sci Technol 14(2):135–151

Oberdörster E (2004) Manufactured nanomaterials (fullerenes, C60) induce oxidative stress in the brain of juvenile largemouth bass. Environ Health Perspect 112:1058–1062

Oberdörster G, Gelein RM, Ferin J, Weiss B (1995) Association of particulate air pollution and acute mortality: involvement of ultrafine particles. Inhal Toxicol 7:111–124

Oberdörster G, Oberdörster E, Oberdörster J (2005) Nanotoxicity: an emerging discipline evolving from studies

of ultrafine particles. Environ Health Perspect 113:823–839

Shin WG, Pui DYH, Fissan H, Neumann S, Trampe A (2007) Calibration and numerical simulation of Nanoparticle Surface Area Monitor (TSI Model 3550 NSAM). J Nanopart Res 9(1):61–69

Shosaku K (2006) Distribution of nanoparticles in the see-through medaka. Environ Health Perspect 114(11):1697–1702

Sinclair D, Countes RJ, Liu BYH, Pui DYH (1976) Experimental verification of the theory of the diffusion battery. J Air Pollut Control Assoc 26:661–663